

Geophysical Research Letters

Supporting Information for

Changes in Atmospheric Convection over the Indo-Pacific Warm Pool and Coupled IOD and ENSO Patterns during the Last Glacial Maximum

Xinquan Zhou^{1,2}, Stéphanie Duchamp-Alphonse², Xiaoxu Shi³, Franck Bassinot⁴, Eva Moreno⁵, Xiaobo Jin¹, Luc Beaufort⁶, Chuanlian Liu¹

¹ State Key Laboratory of Marine Geology, Tongji University, Shanghai, China.

² Université Paris-Saclay, CNRS, GEOPS, Orsay, France.

³ Southern Marine Science and Engineering Guangdong Laboratory (Zhuhai), Zhuhai, China.

⁴ Laboratoire des Sciences du Climat et de l'Environnement, CEA/CNRS/UVSQ, Université Paris-Saclay, Centre CEA-Saclay, Gif-sur-Yvette, France.

⁵ Laboratoire d'Océanographie et du Climat, Sorbonne Université/CNRS/IRD/MNHN, Paris, France.

⁶ Centre de Recherche et d'Enseignement de Géosciences de l'Environnement, CNRS/IRD, Aix-Marseille Université, Aix-en-Provence, France.

Contents of this file

Text S1–S3
Figures S1–S8
Tables S1–S3
References

Text S1. Sediment cores: regional settings and age models

Core BAR94-24

Sediment core BAR94-24 was collected in 1994 by the N/O *Baruna Jaya* during the BARAT cruise. The core site is situated in the southern Andaman Sea, offshore northwestern Sumatra (6.73°N, 94.83°E; water depth: 2676 m), located within the winter biological boom zone near the northern entrance of Malacca Strait (Figure 1; Tan et al., 2006; Lévy et al., 2007). The region experiences seasonal reversals in the surface wind pattern, transitioning from southwesterly winds in summer to northeasterly winds in winter. This shift reflects differences in land-sea thermal contrasts and pressure gradients during summer and winter. The winter northeasterly winds induce coastal upwelling off northwestern Sumatra and Malacca Strait via Ekman transport, elevating net primary productivity (NPP) in these areas. These winter winds are tightly linked to the so-called Northeast Monsoon responsible for increased precipitation across southeast India and Sri Lanka during early winter (Singh and Sontakke, 1999; Nayagam et al., 2009). Interannual variability of the Northeast Monsoon exhibits a strong coupling with the Indian Ocean Dipole (IOD), whereby more vigorous northeasterly winds accompany positive IOD events associated with a weaker Indian Ocean Walker circulation (Kripalani and Kumar, 2004; Prasanna and Yasunari, 2008).

The age model was established through linear interpolation of 9 AMS ^{14}C ages obtained from planktonic foraminifera picked from the core and measured for this study (Table S1). The ^{14}C ages were converted to calendar years using the online software CALIB (version 8.2; <http://calib.org/calib/>), applying the MARINE20 calibration curve. A ΔR value of -131 ± 31 (Southon et al., 2002; <http://calib.org/marine/>) representing the averaged ^{14}C reservoir offset near the core site was applied. Based on the age model, the upper 17–352 cm core section spans ~0.8 to 24 ka, with sedimentation rates ranging from 8 to 20 cm kyr⁻¹ (Figure S1). A total of 168 sediment samples within this interval were used to reconstruct NPP. With sampling every 2 cm, the temporal resolution of the record is between 100 to 250 years.

Core MD98-2152

Sediment core MD98-2152 was collected by the N/O *Marion Dufresne* during the IMAGES-4 cruise in 1998. The core site is located on the southeastern Indian Ocean (6.33°S, 103.88°E; water depth: 1796 m), within the summer biological boom zone off southern Sumatra (Figure 1; Susanto et al., 2001; Lévy et al., 2007). The southeastern Indian Ocean offshore Sumatra experiences seasonally reversal wind, transitioning from southeasterly in summer and autumn to northwesterly in winter, governed by shifting land-sea thermal gradients and pressure patterns. During summer-autumn, the southeasterly winds induce coastal upwelling off southern Sumatra through Ekman transport, elevating NPP in the region. The southeasterly winds comprise a component of the so-called Southeast Monsoon, which traverses the equator and interfaces with the Indian Summer Monsoon (Susanto et al., 2001). Interannual variability in the southeasterly winds over the southeastern Indian Ocean, as well as fluctuations in NPP, exhibit a strong coupling with

the IOD. During positive IOD events characterized by intensified southeasterly winds offshore Sumatra and attenuation of the Indian Ocean Walker circulation, observations indicate elevated NPP in the southeastern Indian Ocean (Lévy et al., 2007; Currie et al., 2013).

The Holocene (the past 11 kyr) age model has been established by a previous study (Zhou et al., 2024). The age model of LGM and the last deglaciation was established through 2 new AMS ^{14}C ages measured on planktonic foraminifera obtained by this study (Table S1). The ^{14}C ages were calibrated to calendar years using a similar approach aforementioned, but with a ΔR value of -117 ± 70 (Southon et al., 2002) specific to this core location. According to the developed age model, the upper 5–393 cm spans ~ 0.6 to 24 ka with sedimentation rates ranging from 6 to 57 cm kyr^{-1} (Figure S1). A total of 195 sediment samples within this section were analyzed to reconstruct NPP. With 2-cm sampling interval, the temporal resolution is between 35 to 313 years. The Holocene portion of NPP record of this core has been published previously (Zhou et al., 2024).

Core MD85-666

Sediment core MD85-666 was collected by the N/O *Marion Dufresne* during the “Indusom” cruise in 1985. The site is located on the equatorial western Indian Ocean, offshore East Africa (Figure 1; 0.17°S , 44.27°E ; water depth: 3045 m). The equatorial western Indian Ocean experiences seasonally reversing cross-equatorial winds that transition from a southerly regime in summer to a northerly flow during winter months. Winds during both seasons can elevate NPP in this region. In summer, the southeasterly winds south of the equator have positive wind stress curl and can induce upwelling associated with an anticyclone, allowing nutrient-rich waters supporting higher NPP to advect northward (Wiggert et al., 2006; Koné et al., 2009). During winter, the northeasterly winds north of the equator also exert positive wind stress curl, potentially spawning upwelling linked to another anticyclone that transports NPP-enhanced waters in a southward direction (Wiggert et al., 2006; Koné et al., 2009).

The age model was established through linear interpolation from 6 AMS ^{14}C ages obtained by this study, measured on planktonic foraminifera (Table S1). The ^{14}C ages were calibrated to calendar years using a similar approach aforementioned, but with a ΔR value of -198 ± 5 (Southon et al., 2002). Per the age model, the upper 2–65 cm section of the core spans ~ 1.2 to 24 ka, with sedimentation rates ranging from 2 to 3 cm kyr^{-1} (Figure S1). A total of 32 sediment samples within section were used to reconstruct NPP variability. With sampling every 2 cm, the temporal resolution of the record is approximately 740 to 922 years.

Core MD98-2178

Sediment core MD98-2178 was collected by the N/O *Marion Dufresne* during the IMAGES-4 cruise in 1998. The site is located on the Celebes Sea, offshore Borneo (Figure 1; 3.62°N , 118.70°E ; water depth: 1984 m). Located within the core region of IPWP, the western Celebes Sea offshore Borneo lies near the mouth of Kayan River in Borneo, and has a near-equatorial locations. These attributes mean both river input nutrients and zonal wind-driven stratification likely influence the NPP variability. Zhou et al. (2023) show co-

varying interannual anomalies between satellite-observed surface chlorophyll-a, zonal winds, and sea surface salinity based on modern observations. As the Kayan River runoff is small, the river input nutrient is taken as a minor effect on the NPP. Easterly low-level winds blowing from land can drive coastal upwelling and nutricline shoaling by pushing seawater offshore. Here, higher NPP corresponds to stronger easterly or weaker westerly winds (Figure 1). Interannual NPP fluctuations also track ENSO phases, with elevated NPP during La Niña events and reduced productivity accompanying El Niño (Figure 1).

The age model has been established by previous studies (Fan et al., 2013, 2018) based on 13 AMS ^{14}C ages measured on planktonic foraminifera. Here, we used these ^{14}C ages to calculate new calendar years based on the approach similar to the above core but using a different ΔR (-64 ± 70) (Southon et al., 2002). According to the age model, the upper 6–1477 cm section spans ~ 1.7 to 24 ka with sedimentation rates ranging from 34 to 172 cm kyr^{-1} (Figure S1). A total of 256 sediment samples within this section were analyzed to reconstruct NPP. With sampling intervals between 4–10 cm, the temporal resolution achieved is approximately 23 to 293 years. The Holocene portion of the NPP record from this core has previously been published in Zhou et al. (2023).

Text S2. Methods: coccolith analysis and SST records

Coccolith analysis

Slides for coccolith analysis were prepared using the “settling” technique (Beaufort et al., 2014; Duchamp-Alphonse et al., 2018) for cores BAR94-24 and MD98-2152, the “simple smearing” method for core MD98-2178, and the “drop” technique (Bordiga et al., 2015; Zhou et al., 2019) for core MD85-666. For each slide, a total of at least 500 coccolith specimens was counted using polarized light microscopes (Leica DM600B and Zeiss Scope A1) at 1,000 \times magnification. Reproducibility and agreement for getting Fp% of each slide preparing method have been proven by a previous study (Lupi et al., 2016).

SST records

In total, we used Mg/Ca data from 43 marine sediment cores from the western equatorial Indian Ocean (WEIO), eastern equatorial Indian Ocean (EEIO), western equatorial Pacific (WEP), central equatorial Pacific (CEP), and eastern equatorial Pacific (EEP) (Table S2; Figure S2). For each SST record, we first obtained the anomalies (SSTA) by subtracting mean values over the early-middle Holocene (EMH; 10–6 ka) following as Dang et al. (2020). Then, all the SST records were linearly interpolated at a regular 0.2 kyr time-interval. The stack curves of SSTA were created by calculating the mean values of different cores at the same ages (Figure S2).

As the SST records from the CEP are sparse and discontinuous in time-series, it is inappropriate to do the stacking for these records. Instead, we operated polynomial fit for these SST values of these records. Then, the SST fit curve was subtracted by mean values over the EMH (10–6 ka) to get the SSTA curve. This strategy was also operated for the other regions (Figure S2). We can see that the equatorial pattern SST values of the fit curves at 0 ka is nearly consistent with that of the observation (Figure S2). The SST in the WEIO is lower than in the EEIO. The SST in the Pacific decreases from the WEP to EEP.

The LGM cooling is quantified by the SSTA difference between LGM (23–19 ka) and late-Holocene (LH; 3-0 ka). As the LH data from CEP are sparse, the cooling is also quantified by the SSTA difference between LGM and EMH.

Text S3. Interpretations on Mg/Ca-temperature of *Pulleniatina obliquiloculata*

Based on previous studies on sediment trap time-series and surface sediments, the calcification depth of *P. obliquiloculata* has been estimated at about 75 m (Mohtadi et al., 2009, 2011). In the sediment trap off Java, the calcification temperatures of *G. ruber* and *P. obliquiloculata* estimated by $\delta^{18}\text{O}$ show seasonality (Figure S7). During the upwelling season (summer-autumn), the calcification temperatures of these two species get closer (Figure S7). Dang et al. (2018) used surface sediments to reconstruct the apparent calcification depth of *P. obliquiloculata* through comparing the foraminifera $\delta^{18}\text{O}$ to the precipitated inorganic carbonate $\delta^{18}\text{O}$ (converted from seawater temperature and salinity). Their results show that the calcification depth of *P. obliquiloculata* has strong seasonality in seasonal coastal upwelling zones, such as the regions offshore southern tip of India and Java (Figure S7). The depth gets shallower during the upwelling seasons. All these facts imply a limitation of the interpretation of ΔT_{Gr-Po} under the “75 m” assumption (see section 3.2 in the main text). A smaller ΔT_{Gr-Po} might not indicate a smaller temperature difference between the mixed-layer and 75 m under a deeper thermocline. Instead, it might reflect getting closer calcification depths of *G. ruber* and *P. obliquiloculata* under a stronger upwelling corresponding to a shallower thermocline (Figure S7).

However, the interpretation of ΔT_{Gr-Po} under the “75 m” assumption is supported by the study on surface sediments offshore Sumatra and Java (Mohtadi et al., 2011). The averaged ΔT_{Gr-Po} in the upwelling core-region is larger than those in the upwelling edge and the non-upwelling region. Therefore, we cannot finally deny that the “75 m” assumption is workable for the comparison between LGM and present, but the “variable depth” assumption has more agreements with our reconstruction on NPP and other proxy evidence (see section 3.2 in the main text).

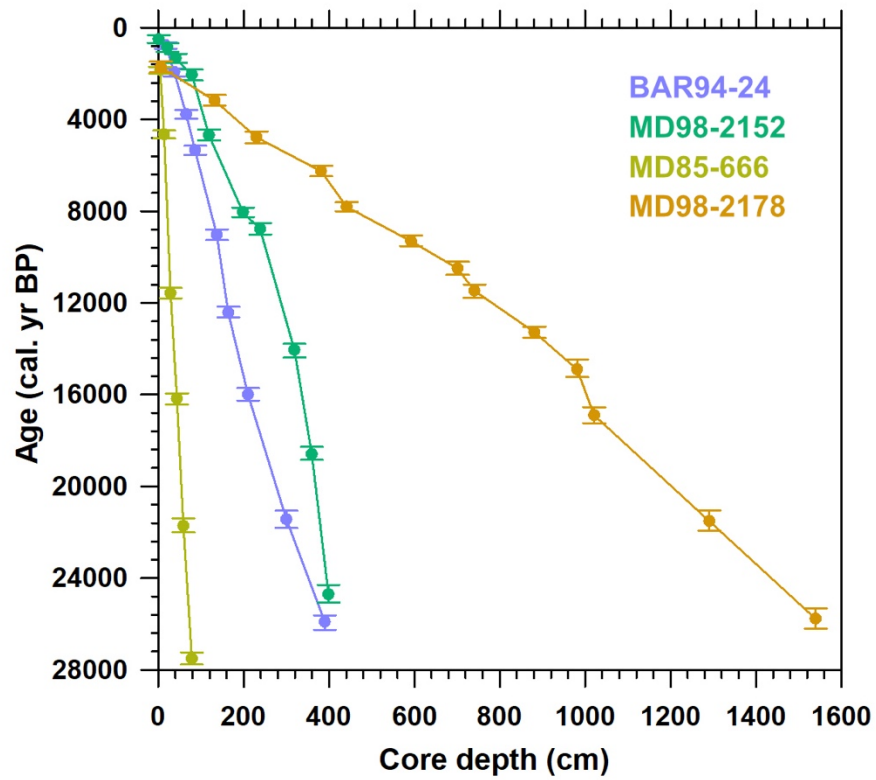


Figure S1. Age-depth relationships of the 4 studied cores (Table S1). The dots mark the calendar age medians. The error bars mark the calendar age 2σ .

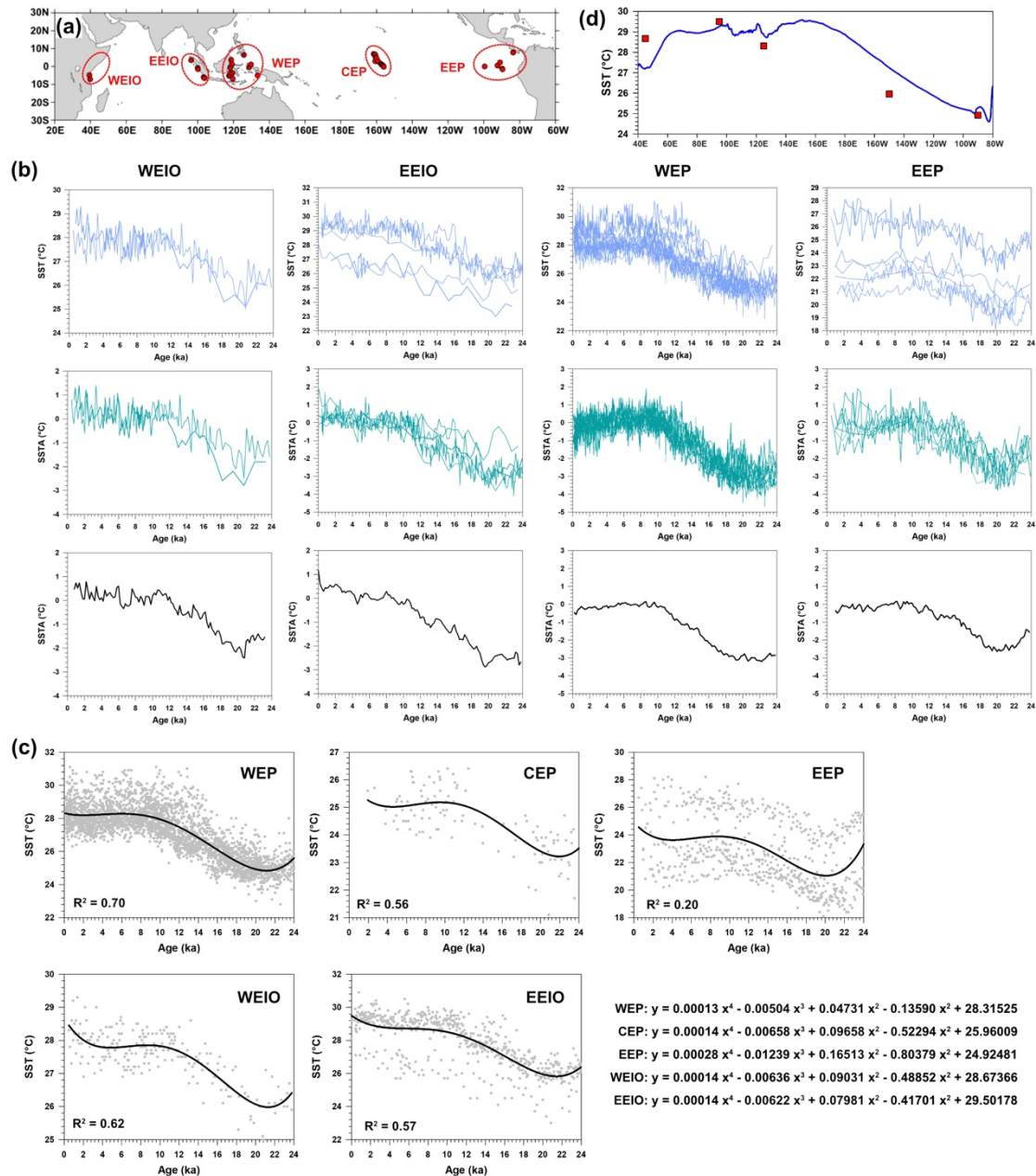


Figure S2. (a) Locations of the published Mg/Ca-SST records in the equatorial regions (Table S2). (b) SST, SSTA records and the SSTA stacks (Text S2). (c) Polynomial fitting of SST records. (d) Modern SST in the equatorial (10°S–10°N) region (blue curve) and the SST of polynomial fitting at 0 ka (red points). Modern SST data is from NOAA OI SST V2 (1992–2019; <https://psl.noaa.gov/data/gridded/data.noaa.oisst.v2.highres.html>).

AWI-ESM LGM-PI

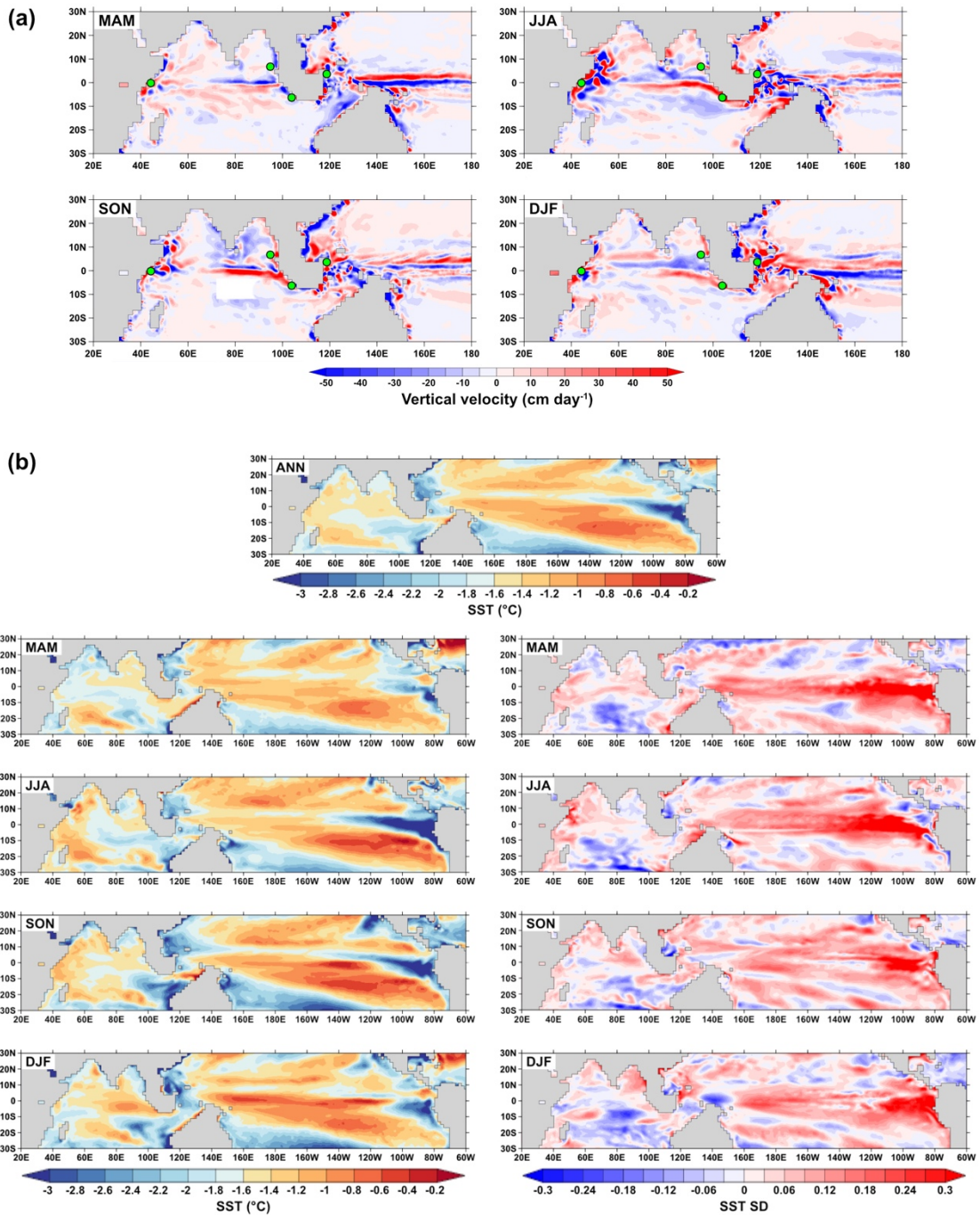


Figure S3. Changes between LGM and PI simulated by AWI-ESM. (a) Seasonal mean vertical velocity averaged over the upper 100 m seawater (unit: cm day^{-1}). The green dots mark the core locations of NPP reconstruction. (b) Annual and seasonal SST mean sea surface temperature (SST; unit: $^{\circ}\text{C}$), and standard deviation (SD) of seasonal SST.

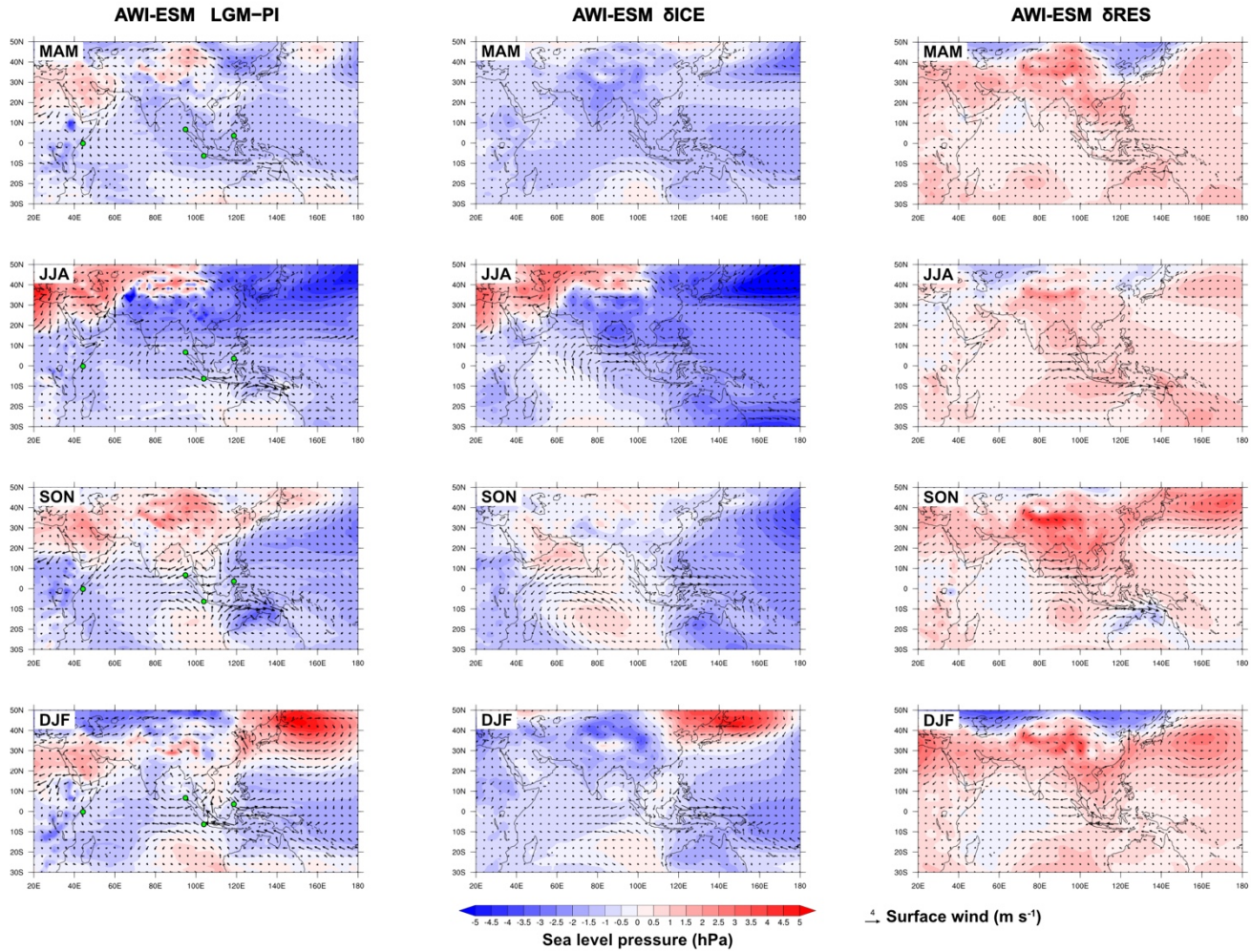


Figure S4. Changes due to LGM conditions and larger ice sheet and the rest changes simulated by the LGM and sensitivity experiments run with AWI-ESM. Seasonal mean sea level pressure (unit: hPa) and surface wind (vectors; unit: m s⁻¹) are shown. The pressure results are calibrated by subtracting the global mean values.

LGM-PI Annual

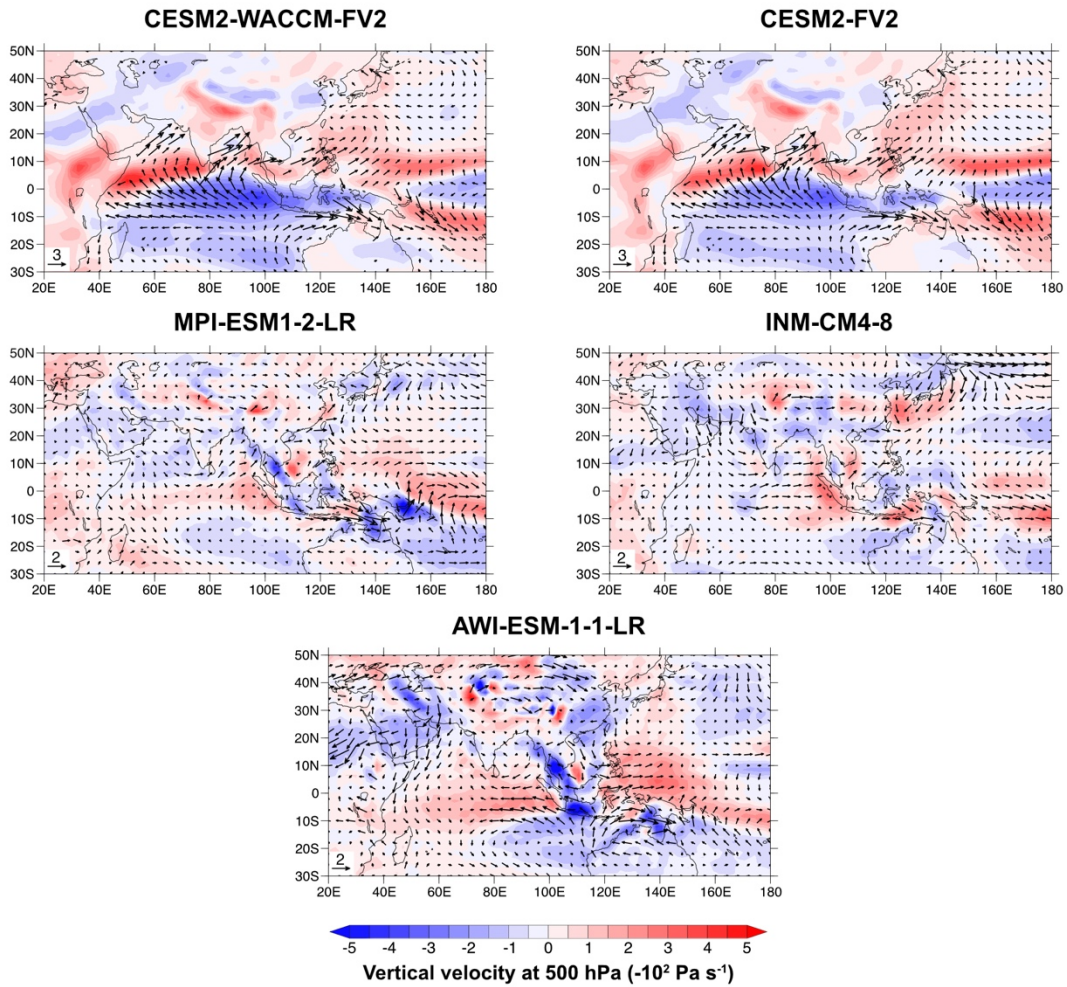


Figure S5. Simulated difference of surface wind (m s^{-1}) or 1000 hPa wind (for CESM2-WACCM-FV2 and CESM2-FV2) and vertical velocity at 500 hPa between the LGM and preindustrial.

AWI-ESM

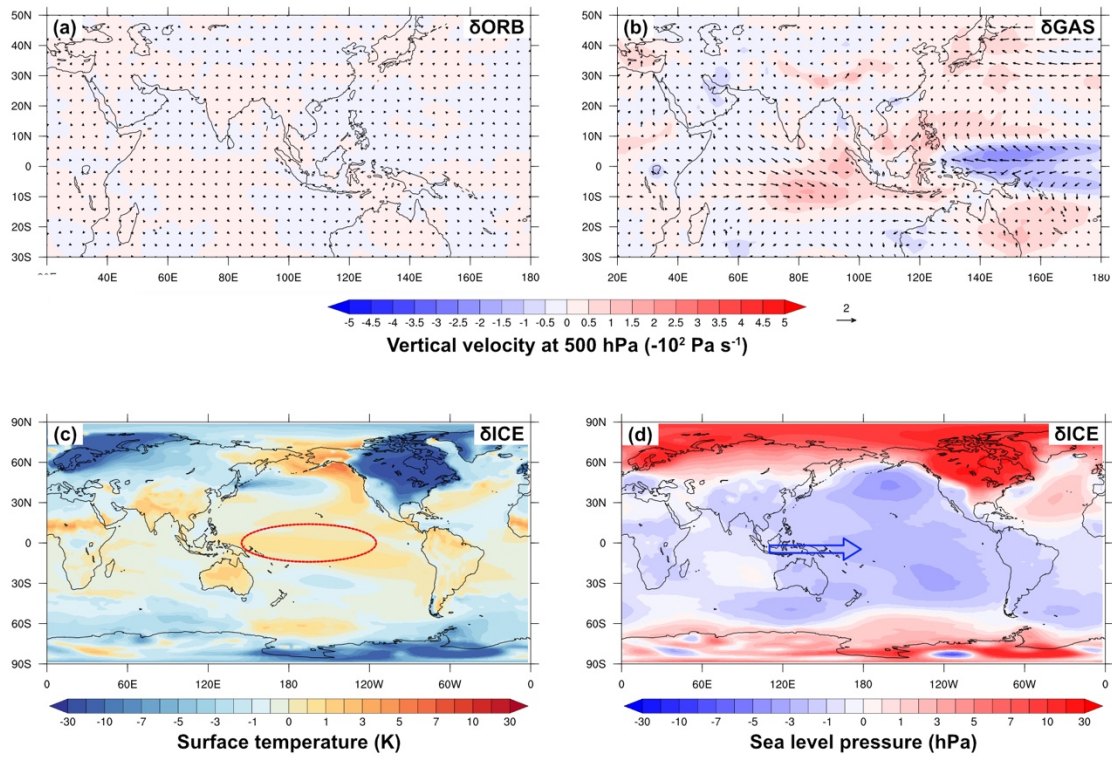


Figure S6. (a and b) Annual mean vertical velocity at the 500 hPa atmospheric level (-10^2 Pa s^{-1}) and surface wind (m s^{-1}) simulated by AWI-ESM sensitivity experiments (δORB and δGAS). (c and d) Changes in atmosphere surface temperature (unit: K) sea level pressure (hPa) due to larger ice sheets (δICE). The pressure results are calibrated by subtracting the global mean values. The red circle on (c) marks the anomalous warming and the blue arrow on (d) marks the anomalous pressure gradient and westerly wind.

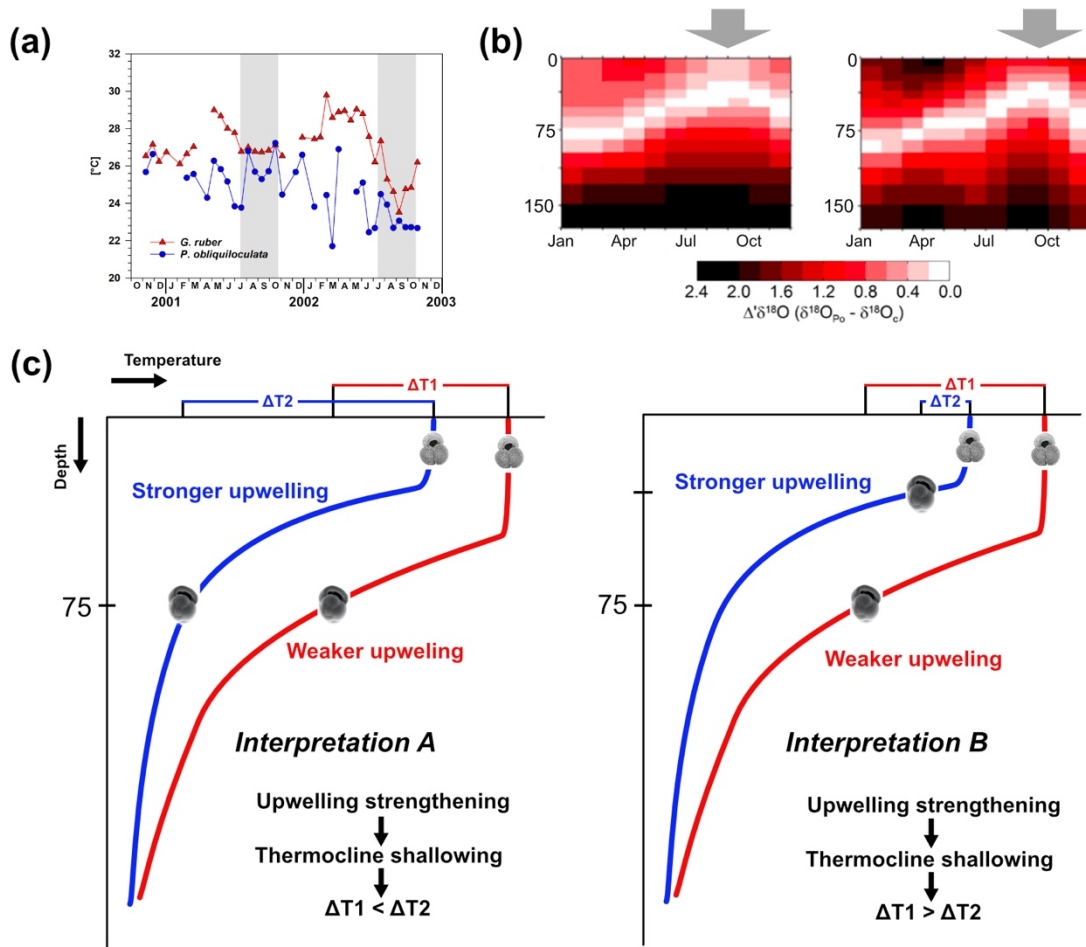


Figure S7. (a) Estimated calcification temperatures of *G. ruber* and *P. obliquiloculata* (modified from Mohtadi et al., 2009). The gray bars mark the upwelling season (b) Estimated calcification depth ($\Delta\delta^{18}\text{O} = 0$) of *P. obliquiloculata* (modified from Dang et al., 2018). The $\Delta\delta^{18}\text{O}$ is the difference between *P. obliquiloculata* $\delta^{18}\text{O}$ and precipitated inorganic carbonate $\delta^{18}\text{O}$ in the regions offshore southern tip of India and Java. The arrows mark the upwelling season. (c) Schematic diagram of the two interpretations on ΔT_{Gr-Po} .

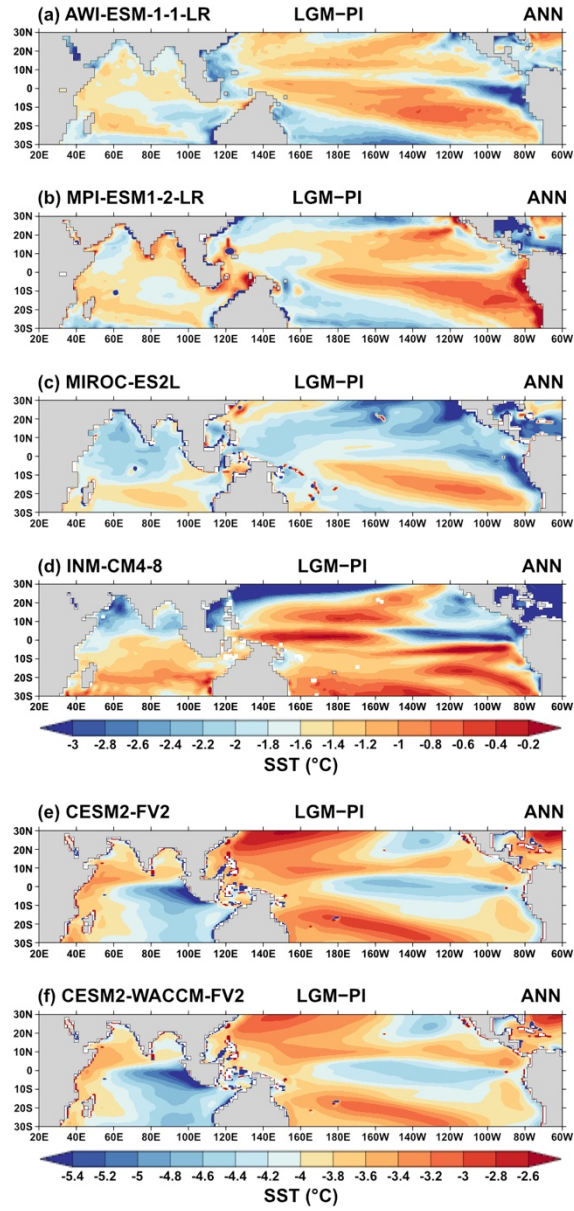


Figure S8. Changes (difference between LGM and PI) in SST simulated by PMIP4 models.

Table S1. Radiocarbon (^{14}C) and calibrated ages of the 4 studied cores. Calendar years are the years before 1950 AD. ΔR used for the calendar year calibration are averages of ^{14}C reservoir offsets of sites near the core locations (Southon et al., 2002; <http://calib.org/marine/>). *G. ruber* = *Globigerinoides ruber*; *G. sacculifer* = *Globigerinoides sacculifer*.

BAR94-24 ($\Delta\text{R} = -133 \pm 31$)							
Depth (cm)	Materials	^{14}C age (yr)	^{14}C age error (yr)	^{14}C age source	Calendar age median (yr)	Calendar age lower 2σ (yr)	Calendar age upper 2σ (yr)
17	<i>G. ruber</i>	1240	35	This study	760	631	912
37.5	<i>G. ruber</i>	2335	30	This study	1942	1764	2119
65.5	<i>G. ruber</i>	3830	35	This study	3779	3585	3969
86	<i>G. ruber</i>	5040	40	This study	5346	5140	5535
137	<i>G. ruber</i>	8450	50	This study	9033	8797	9259
164	<i>G. ruber</i>	10930	50	This study	12429	12165	12628
210	<i>G. ruber</i> + <i>G. sacculifer</i>	13800	60	This study	15997	15717	16267
300	<i>G. ruber</i> + <i>G. sacculifer</i>	18340	90	This study	21444	21058	21815
390	<i>G. ruber</i> + <i>G. sacculifer</i>	22420	130	This study	25908	25627	26256
MD98-2152 ($\Delta\text{R} = -117 \pm 70$)							
Depth (cm)	Materials	^{14}C age (yr)	^{14}C age error (yr)	^{14}C age source	Calendar age median (yr)	Calendar age lower 2σ (yr)	Calendar age upper 2σ (yr)
1	<i>G. ruber</i> + <i>G. sacculifer</i>	960	30	Zhou et al. (2024)	511	323	661
21	<i>G. ruber</i> + <i>G. sacculifer</i>	1360	30	Zhou et al. (2024)	859	670	1056
41	<i>G. ruber</i> + <i>G. sacculifer</i>	1820	30	Zhou et al. (2024)	1336	1137	1536
78.5	<i>G. ruber</i> + <i>G. sacculifer</i>	2440	30	Zhou et al. (2024)	2056	1828	2297
118.5	<i>G. ruber</i> + <i>G. sacculifer</i>	4540	30	Zhou et al. (2024)	4688	4431	4910
198.5	<i>G. ruber</i> + <i>G. sacculifer</i>	7640	30	Zhou et al. (2024)	8042	7838	8258
238.5	<i>G. ruber</i> + <i>G. sacculifer</i>	8280	30	Zhou et al. (2024)	8772	8520	9009
318.5	<i>G. ruber</i> + <i>G. sacculifer</i>	12490	30	Zhou et al. (2024)	14052	13769	14370
359.5	<i>G. ruber</i> + <i>G. sacculifer</i>	15990	60	This study	18601	18277	18843
398.5	<i>G. ruber</i> + <i>G. sacculifer</i>	21270	100	This study	24712	24301	25079

(Continued)

MD85-666 ($\Delta R = -98 \pm 5$)

Depth (cm)	Materials	^{14}C age (yr)	^{14}C age error (yr)	^{14}C age source	Calendar age median (yr)	Calendar age lower 2σ (yr)	Calendar age upper 2σ (yr)
4.5	<i>G. ruber</i> + <i>G. sacculifer</i>	2300	30	This study	1855	1699	2004
13.5	<i>G. ruber</i> + <i>G. sacculifer</i>	4520	30	This study	4649	4480	4818
28.5	<i>G. ruber</i> + <i>G. sacculifer</i>	10405	35	This study	11568	11342	11793
43.5	<i>G. ruber</i> + <i>G. sacculifer</i>	13980	45	This study	16184	15944	16432
58.5	<i>G. ruber</i> + <i>G. sacculifer</i>	18590	70	This study	21728	21403	22010
78.5	<i>G. ruber</i> + <i>G. sacculifer</i>	24100	130	This study	27512	27235	27769

MD98-2178 ($\Delta R = -64 \pm 70$)

Depth (cm)	Materials	^{14}C age (yr)	^{14}C age error (yr)	^{14}C age source	Calendar age median (yr)	Calendar age lower 2σ (yr)	Calendar age upper 2σ (yr)
6	<i>G. ruber</i>	2210	40	Fan et al. (2013)	1707	1473	1946
132	<i>G. ruber</i>	3400	30	Fan et al. (2013)	3168	2924	3389
230	<i>G. ruber</i>	4665	30	Fan et al. (2013)	4777	4522	5027
381	<i>G. ruber</i>	5965	35	Fan et al. (2013)	6257	6018	6469
441	<i>G. ruber</i>	7470	40	Fan et al. (2013)	7810	7608	8002
592	<i>G. ruber</i>	8745	50	Fan et al. (2013)	9302	9049	9513
701	<i>G. ruber</i>	9675	55	Fan et al. (2013)	10493	10208	10778
741	<i>G. ruber</i>	10370	55	Fan et al. (2013)	11469	11194	11785
881	<i>G. ruber</i>	11885	80	Fan et al. (2013)	13271	13024	13525
981	<i>G. ruber</i>	13040	70	Fan et al. (2018)	14896	14468	15238
1021	<i>G. ruber</i>	14580	80	Fan et al. (2018)	16899	16555	17245
1291	<i>G. ruber</i>	18470	120	Fan et al. (2018)	21521	21057	21950
1540	<i>G. ruber</i>	22340	180	Fan et al. (2018)	25774	25325	26211

Table S2. List of published Mg/Ca-SST records

Core ID	Region	Latitude	Longitude	Reference
GeoB12610-2	WEIO	-4.82	39.42	Rippert et al., 2015
GeoB12615-4	WEIO	-7.14	39.84	Romahn et al., 2014
SO189-119KL	EEIO	3.52	96.31	Mohtadi et al., 2014
SO189-39KL	EEIO	-0.79	99.91	Mohtadi et al., 2014
GeoB10029-4	EEIO	-1.49	100.13	Mohtadi et al., 2010
GeoB10038-4	EEIO	-5.94	103.27	Mohtadi et al., 2010
SO139-74KL	EEIO	-6.54	103.83	Wang et al., 2018
MD98-2161	WEP	-5.21	117.48	Fan et al., 2018
MD98-2162	WEP	-4.68	117.90	Visser et al., 2003
GIK18519	WEP	-0.57	118.11	Schröder et al., 2018
GIK18526	WEP	-3.61	118.17	Schröder et al., 2018
MD98-2178	WEP	3.62	118.70	Fan et al., 2018
GIK18522	WEP	1.40	119.08	Schröder et al., 2018
GIK18515	WEP	-3.63	119.36	Schröder et al., 2016
GIK18540	WEP	-6.87	119.58	Schröder et al., 2018
MD98-2181	WEP	6.45	125.83	Stott et al., 2002
MD10-3340	WEP	-0.52	128.72	Dang et al., 2020
MD01-2386	WEP	1.13	129.79	Jian et al., 2020
MD01-2176	WEP	-5.00	133.45	Stott et al., 2007
ML1208-37BB	CEP	7.04	-161.63	Monteagudo et al., 2021
ML1208-37BB/39MC	CEP	6.83	-161.04	Monteagudo et al., 2021
ML1208-06BB	CEP	6.41	-161.01	Monteagudo et al., 2021
ML1208-34BB	CEP	5.62	-160.79	Monteagudo et al., 2021
ML1208-29MC	CEP	2.97	-160.77	Monteagudo et al., 2021
ML1208-09MC	CEP	6.40	-160.77	Monteagudo et al., 2021
ML1208-35BB	CEP	6.67	-160.73	Monteagudo et al., 2021
ML1208-32BB/33MC	CEP	5.20	-160.43	Monteagudo et al., 2021
ML1208-31BB	CEP	4.68	-160.05	Monteagudo et al., 2021
ML1208-27BB	CEP	2.77	-159.29	Monteagudo et al., 2021
ML1208-28BB	CEP	2.97	-159.20	Monteagudo et al., 2021
ML1208-11GC	CEP	1.47	-157.58	Monteagudo et al., 2021
ML1208-20BB/11GC	CEP	1.27	-157.26	Monteagudo et al., 2021
ML1208-19GC	CEP	0.83	-156.87	Monteagudo et al., 2021
ML1208-18GC	CEP	0.59	-156.66	Monteagudo et al., 2021
ML1208-15GC	CEP	0.16	-156.12	Monteagudo et al., 2021

(Continued)

ML1208-13BB/14MC	CEP	-0.22	-155.96	Monteagudo et al., 2021
ODP1240	EEP	0.02	-99.54	Pena et al., 2008
TR163-22	EEP	0.52	-92.40	Lea et al., 2006
TR163-19	EEP	2.26	-90.95	Lea et al., 2000
V21-30	EEP	-1.22	-89.68	Koutavas and Joanides, 2012
CD38-17P	EEP	-1.60	-89.57	Sadekov et al., 2013
ME0005A-43JC	EEP	7.86	-83.61	Benway et al., 2006
ODP1242	EEP	7.86	-83.61	Benway et al., 2006

Table S3. List of PMIP4 models

Model	Atmospheric resolution (lat×lon)	Model reference
AWI-ESM-1-1-LR	96×192	Sidorenko et al. (2015)
CESM2-FV2	96×144	Zhu et al. (2022a)
CESM2-WACCM-FV2	96×144	Zhu et al. (2022b)
INM-CM4-8	120×180	Volodin et al. (2018)
MIROC-ES2L	64×128	Hajima et al. (2020)
MPI-ESM1-2-LR	96×192	Mauritsen et al. (2019)

References

- Beaufort, L., Barbarin, N., & Gally, Y. (2014). Optical measurements to determine the thickness of calcite crystals and the mass of thin carbonate particles such as coccoliths. *Nature Protocols*, 9, 633–642.
- Bordiga, M., Bartol, M., & Henderiks, J. (2015). Absolute nannofossil abundance estimates: quantifying the pros and cons of different techniques. *Revue de micropaéontologie*, 58, 155–165.
- Benway, H. M., Mix, A. C., Haley, B. A., & Klinkhammer, G. P. (2006). Eastern Pacific Warm Pool paleosalinity and climate variability: 0–30 kyr. *Paleoceanography*, 21, PA3008.
- Currie, J. C., Lengaigne, M., Vialard, J., Kaplan, D. M., Aumont, O., Naqvi, S. W. A., & Maury, O. (2013). Indian Ocean Dipole and El Niño/Southern Oscillation impacts on regional chlorophyll anomalies in the Indian Ocean. *Biogeosciences*, 10, 6677–6698.
- Duchamp-Alphonse, S., Siani, G., Michel, E., Beaufort, L., Gally, Y., & Jaccard, S. L. (2018). Enhanced ocean-atmosphere carbon partitioning via the carbonate counter pump during the last deglacial. *Nature Communication*, 9, 2396.
- Dang, H., Jian, Z., Wang, Y., Mohtadi, M., Rosenthal, Y., Ye, L., Bassinot, F., & Kuhnt, W. (2020). Pacific warm pool subsurface heat sequestration modulated Walker circulation and ENSO activity during the Holocene. *Science Advances*, 6, eabc0402.
- Dang, H., Jian, Z., Wu, J., Bassinot, F., Wang, T., & Kissel, C. (2018). The calcification depth and Mg/Ca thermometry of *Pulleniatina obliquiloculata* in the tropical Indo-Pacific: A core-top study. *Marine Micropaleontology*, 145, 28–40.
- Fan, W., Jian, Z., Bassinot, F., & Chu, Z. (2013). Holocene centennial-scale changes of the Indonesian and South China sea throughflows: evidences from the Makassar Strait. *Global and Planetary Change*, 111, 111–117.
- Fan, W., Jian, Z., Chu, Z., Dang, H., Wang, Y., Bassinot, F., Han, X., & Bian, Y. (2018). Variability of the Indonesian Throughflow in the Makassar Strait over the last 30 ka. *Scientific Reports*, 8, 5678.
- Hajima, T., Watanabe, M., Yamamoto, A., Tatebe, H., Noguchi, M.A., Abe, M., Ohgaito, R., Ito, A., Yamazaki, D., Okajima, H., Ito, A., Takata, K., Ogochi, K., Watanabe, S., & Kawamiya, M. (2020). Development of the MIROC-ES2L Earth system model and the evaluation of biogeochemical processes and feedbacks. *Geoscientific Model Development*, 13, 2197–2244.
- Jian, Z., Wang, Y., Dang, H., Lea, D. W., Liu, Z., Jin, H., & Yin, Y. (2020). Half-precessional cycle of thermocline temperature in the western equatorial Pacific and its bihemispheric dynamics. *Proceedings of the National Academy of Sciences*, 117, 7044–7051. <https://doi.org/10.1073/pnas.1915510117>
- Koné, V., Aumont, O., Lévy, M., & Resplandy, L. (2009). Physical and biogeochemical controls of the phytoplankton seasonal cycle in the Indian Ocean: A model study. In Wigger, J. D., Hood, R. R., Naqvi, S. W. A., Brink, K. H., & Smith, S. L. (Eds.), *Indian Ocean Biogeochemical Processes and Ecological Variability. Geophysical Monograph Series*, 185, 9–32.
- Koutavas, A., & Joannides, S. (2012). El Niño-Southern Oscillation extreme in the Holocene and Last Glacial Maximum. *Paleoceanography*, 27, PA4208
- Kripalani, R. H., & Kumar, P. (2004). Northeast monsoon rainfall variability over south peninsular India vis-à-vis the Indian Ocean dipole mode. *International Journal of Climatology*, 24, 1267–1282.
- Lea, D. W., Pak, D. K., & Spero, H. J. (2000). Climate impact of late Quaternary equatorial Pacific sea surface temperature variations. *Science*, 289, 1719–1724.

- Lea, D. W., Pak, D. K., Belanger, C. L., Spero, H. J., Hall, M. A., & Shackleton, N. J. (2006). Paleoclimate history of Galápagos surface waters over the last 135,000 yr. *Quaternary Science Reviews*, 25, 1152–1167.
- Lévy, M., Shankar, D., André, J.-M., Shenoi, S. S., Durand, F., & de Boyer Montégut, C. (2007). Basin-wide seasonal evolution of the Indian Ocean's phytoplankton blooms. *Journal of Geophysical Research*, 112, C12012.
- Lupi, C., Bordiga, M., Sacchi, R., Galinetto, P., Beaufort, L., & Cobianchi, M. (2016). Do sample preparation techniques affect the relative abundance of *Florisphaera profunda*? *Marine Micropaleontology*, 127, 42–49. <http://dx.doi.org/10.1016/j.marmicro.2016.07.007>
- Mauritsen, T., Bader, J., Becker, T., Behrens, J., Bittner, M., Brokopf, R., Brovkin, V., Claussen, M., Crueger, T., Esch, M., Fast, I., Fiedler, S., Flaßchner, D., Gayler, V., Giorgetta, M., Goll, D.S., Haak, H., Hagemann, S., Hedemann, C., Hohenegger, C., Ilyina, T., Jahns, T., Jimenéz-de-la-Cuesta, D., Jungclaus, J., Kleinen, T., Kloster, S., Kracher, D., Kinne, S., Kleberg, D., Lasslop, G., Kornblueh, L., Marotzke, J., Matei, D., Meraner, K., Mikolajewicz, U., Modali, K., Mo'bis, B., Müller, W.A., Nabel, J.E.M.S., Nam, C.C.W., Notz, D., Nyawira, S.-S., Paulsen, H., Peters, K., Pincus, R., Pohlmann, H., Pongratz, J., Popp, M., Raddatz, T.J., Rast, S., Redler, R., Reick, C.H., Rohrschneider, T., Schemann, V., Schmidt, H., Schnur, R., Schulzweida, U., Six, K.D., Stein, L., Stemmler, I., Stevens, B., von Storch, J.-S., Tian, F., Voigt, A., Vrese, P., Wieners, K.-H., Wilkenskjaeld, S., Winkler, A., & Roeckner, E. (2019). Developments in the MPI-M Earth System Model version 1.2 (MPI-ESM1.2) and its response to increasing CO₂. *Journal of Advances in Modeling Earth Systems*, 11, 998–1038.
- Monteagudo, M. M., Lynch-Stieglitz, J., Marchitto, T. M., & Schmidt, M. W. (2021). Central equatorial Pacific cooling during the Last Glacial Maximum. *Geophysical Research Letters*, 48, e2020GL088592.
- Mohtadi, M., Steinke, S., Groeneveld, J., Fink, H. G., Rixen, T., Hebbeln, D., Donner, B., & Herunadi, B. (2009). Low-latitude control on seasonal and interannual changes in planktonic foraminiferal flux and shell geochemistry off south Java: A sediment trap study. *Paleoceanography*, 24, PA1201.
- Mohtadi, M., Steinke, S., Lückge, A., Groeneveld, J., & Hathorne, E. D. (2010). Glacial to Holocene surface hydrography of the tropical eastern Indian Ocean. *Earth and Planetary Science Letters*, 292, 89–97.
- Mohtadi, M., Oppo, D. W., Lückge, A., De Pol-Holz, R., Steinke, S., Groeneveld, J., Hemme, N., & Hebbeln, D. (2011). Reconstructing the thermal structure of the upper ocean: Insights from planktonic foraminifera shell chemistry and alkenones in modern sediments of the tropical eastern Indian Ocean. *Paleoceanography*, 26, PA3219.
- Mohtadi, M., Prange, M., Oppo, D. W., De Pol-Holz, R., Merkel, U., Zhang, X., Steinke, S., & Lückge, A. (2014). North Atlantic forcing of tropical Indian Ocean climate. *Nature*, 509, 76–80.
- Nayagam, L. R., Janardanan, R., & Mohan, H. S. R. (2009). Variability and teleconnectivity of the northeast monsoon rainfall over India. *Global and Planetary Change*, 69, 225–231.
- Pena, L. D., Cacho, I., Ferretti, P., & Hall, M. A. (2008). El Niño–Southern Oscillation–like variability during glacial terminations and interlatitudinal teleconnections. *Paleoceanography*, 23, PA3101.
- Prasanna, V., & Yasunari, T., 2008. Interannual variability of atmospheric water balance over South Peninsular India and Sri Lanka during the northeast monsoon season. *International Journal of Climatology*, 28, 1997–2009.
- Rippert, N., Baumann, K.-H., & Pätzold, J. (2015). Thermocline fluctuations in the western tropical Indian Ocean during the past 35 ka. *Journal of Quaternary Science*, 30, 201–210.

- Romahn, S., Mackensen, A., Groeneveld, J., & Pätzold, J. (2014). Deglacial intermediate water reorganization: new evidence from the Indian Ocean. *Climate of the Past*, 10, 293–303.
- Sadekov, A. Y., Ganeshram, R., Pichevin, L., Berdin, R., McClymont, E., Elderfield, H., & Tudhope, A. W. (2013). Palaeoclimate reconstructions reveal a strong link between El Niño–Southern Oscillation and Tropical Pacific mean state. *Nature Communications*, 4, 2692. <https://doi.org/10.1038/ncomms3692>
- Susanto, R. D., Gordon, A. L., Zheng, Q., 2001. Upwelling along the coasts of Java and Sumatra and its relation to ENSO. *Geophysical Research Letters*, 28, 1599–1602.
- Southon, J., Kashgarian, M., Fontugne, M., Metivier, B., & Yim, W. W.-S. (2002). Marine reservoir corrections for the Indian Ocean and southeast Asia. *Radiocarbon*, 44, 167–180.
- Schröder, J. F., Holbourn, A., Kuhnt, W., & Küssner, K. (2016). Variations in sea surface hydrology in the southern Makassar Strait over the past 26 kyr. *Quaternary Science Reviews*, 154, 143–156.
- Schröder, J. F., Kuhnt, W., Holbourn, A., Beil, S., Zhang, P., Hendrizon, M. & Xu, J. (2018), Deglacial Warming and Hydroclimate Variability in the Central Indonesian Archipelago. *Paleoceanography and Paleoclimatology*, 33, 974–993.
- Stott, L., Poulsen, C., Lund, S., & Thunell, R. (2002). Super ENSO and global climate oscillations at millennial time scales. *Science*, 297, 222–226.
- Stott, L., Timmermann, A., & Thunell, R. (2007). Southern Hemisphere and deep-sea warming led deglacial atmospheric CO₂ rise and tropical warming. *Science*, 318, 435–438.
- Singh, N., & Sontakke, N.A. (1999). On the variability and prediction of rainfall in the post-monsoon season over India. *International Journal of Climatology*, 19, 309–339.
- Sidorenko, D., Rackow, T., Jung, T., Semmler, T., Barbi, D., Danilov, S., Dethloff, K., Dorn, W., Fieg, K., Goessling, H.F., Handorf, D., Harig, S., Hiller, W., Juricke, S., Losch, M., Schröter, J., Sein, D.V., & Wang, Q. (2015). Towards multi-resolution global climate modeling with ECHAM6–FESOM. Part I: model formulation and mean climate. *Climate Dynamics*, 44, 757–780.
- Tan, C. K., Ishizaka, J., Matsumura, S., Yusoff, F. M., & Mohamed, M. I. H. (2006). Seasonal variability of SeaWiFS chlorophyll a in the Malacca Straits in relation to Asian monsoon. *Continental Shelf Research*, 26, 168–178.
- Volodin, E.M., Mortikov, E.V., Kostykin, S.V., Galin, V.Y., Lykossov, V.N., Gritsun, A.S., Diansky, N.A., Gusev, A.V., Iakovlev, N.G., Shestakova, A.A., & Emelina, S.V. (2018). Simulation of the modern climate using the INM-CM48 climate model. *Russian Journal of Numerical Analysis and Mathematical Modelling*, 33, 367–374.
- Visser, K., Thunell, R., & Stott, L. (2003). Magnitude and timing of temperature change in the Indo-Pacific warm pool during deglaciation. *Nature*, 421, 152–155.
- Wiggert, J. D., Murtugudde, R. G., & Christian, J. R. (2006). Annual ecosystem variability in the tropical Indian Ocean: Results of a coupled bio-physical ocean general circulation model. *Deep-Sea Research II*, 53, 644–676.
- Wang, X., Jian, Z., Lückge, A., Wang, Y., Dang, H., & Mohtaid, M. (2018). Precession-paced thermocline water temperature changes in response to upwelling conditions off southern Sumatra over the past 300,000 years. *Quaternary Science Reviews*, 192, 123–134.
- Zhu, J., Otto-Bliesner, B. L., Brady, E. C., Gettelman, A., Bacmeister, J. T., Neale, R. B., Poulsen, C. J., Shaw, J. K., McGraw, Z. S., & Kay, J. E. (2022a). LGM paleoclimate constraints inform cloud parameterizations and equilibrium climate sensitivity in CESM2. *Journal of Advances in Modeling Earth Systems*, 14, e2021MS002776.
- Zhu, J., Otto-Bliesner, B. L., Garcia, R., Brady, E. C., Mills, M., Kinnison, D., & Lamarque, J.-F. (2022b). Small impact of stratospheric dynamics and chemistry on the surface temperature of the Last Glacial Maximum in CESM2(WACCM6ma). *Geophysical Research Letters*, 49, e2022GL099875.

- Zhou, X., Jin, X., Shi, X., & Liu, C. (2023). The change in convection over the Indo-Pacific warm pool in the mid-Holocene and its influence on South Asian precipitation. *Quaternary Science Reviews*, 322, 108399.
- Zhou, X., Duchamp-Alphonse, S., Bassinot, F., & Liu, C. (2024). Summer and autumn insolation as the pacemaker of surface wind and precipitation dynamics over tropical Indian Ocean during the Holocene: Insights from paleoproductivity records and paleoclimate simulations. *Paleoceanography and Paleoclimatology*, 39, e2023PA004786.
- Zhou, X., Jin, X., Shi, X., Liu, C. & 2024. The change in convection over the Indo-Pacific warm pool in the mid-Holocene and its influence on South Asian precipitation. *Quaternary Science Reviews*, 322, 108399.